Integration of microwave tomography with magnetic resonance for improved breast imaging

Paul M. Meaney[a)]
Thayer School of Engineering, Dartmouth College, Hanover, New Hampshire 03755

Amir H. Golnabi
Massachusetts General Hospital, Boston, Massachusetts 02114 and Harvard Medical School, Boston, Massachusetts 02115

Neil R. Epstein
Thayer School of Engineering, Dartmouth College, Hanover, New Hampshire 03755

Shireen D. Geimer
Department of Radiology, Geisel School of Medicine, Dartmouth College, Hanover, New Hampshire 03755

Margaret W. Fanning
Thayer School of Engineering, Dartmouth College, Hanover, New Hampshire 03755

John B. Weaver
Department of Radiology, Geisel School of Medicine, Dartmouth College, Hanover, New Hampshire 03755

Keith D. Paulsen
Thayer School of Engineering, Dartmouth College, Hanover, New Hampshire 03755; Department of Radiology, Geisel School of Medicine, Dartmouth College, Hanover, New Hampshire 03755; Norris Cotton Cancer Center, Dartmouth Hitchcock Medical Center, Lebanon, New Hampshire 03756; and Advanced Surgical Center, Dartmouth Hitchcock Medical Center, Lebanon, New Hampshire 03756

(Received 4 April 2013; revised 6 August 2013; accepted for publication 11 August 2013; published 12 September 2013)

Purpose: Breast magnetic resonance imaging is highly sensitive but not very specific for the detection of breast cancer. Opportunities exist to supplement the image acquisition with a more specific modality provided the technical challenges of meeting space limitations inside the bore, restricted breast access, and electromagnetic compatibility requirements can be overcome. Magnetic resonance (MR) and microwave tomography (MT) are complementary and synergistic because the high resolution of MR is used to encode spatial priors on breast geometry and internal parenchymal features that have distinct electrical properties (i.e., fat vs fibroglandular tissue) for microwave tomography.
Methods: The authors have overcome integration challenges associated with combining MT with MR to produce a new coregistered, multimodality breast imaging platform—magnetic resonance microwave tomography, including: substantial illumination tank size reduction specific to the confined MR bore diameter, minimization of metal content and composition, reduction of metal artifacts in the MR images, and suppression of unwanted MT multipath signals.
Results: MR SNR exceeding 40 dB can be obtained. Proper filtering of MR signals reduces MT data degradation allowing MT SNR of 20 dB to be obtained, which is sufficient for image reconstruction. When MR spatial priors are incorporated into the recovery of MT property estimates, the errors between the recovered versus actual dielectric properties approach 5%.
Conclusions: The phantom and human subject exams presented here are the first demonstration of combining MT with MR to improve the accuracy of the reconstructed MT images. © *2013 American Association of Physicists in Medicine*. [http://dx.doi.org/10.1118/1.4820361]

Key words: breast cancer, MRI, microwave tomography, multimodal imaging, specificity enhancement

1. INTRODUCTION

Clinically, MR is the most sensitive exam for cancer surveillance especially in the dense breast.[1–5] Indeed, national guidelines now recommend regular breast MR screening exams in women with an elevated lifetime breast cancer risk of 20% or more.[6] Breast MR has been used successfully to monitor treatment response to neoadjuvant chemotherapy and is deployed routinely for cancer staging and surgical treatment planning.[7,8] Thus, even with pressures from healthcare cost containment, the emergence of x-ray tomographic systems[9–11] and the relative expense of an exam, the number of breast MR studies is likely to continue to grow in the future because of their exquisite soft-tissue delineation. However, breast MR has a substantial false positive rate—13% to 19%[12,13]—and it is imperfect when used to monitor treatment or follow the breast for recurrence[14,15] due to its reliance on gadolinium as a nonspecific contrast agent. The number of false positives

caused by the technique is particularly troubling because of the clinical management burden that is created by the increase in contrast-enhancing foci that need to be evaluated. In addition, in a limited number of patients with kidney disease, the toxicity side effects from the gadolinium are a significant health risk.[16] As a result, opportunities exist to supplement the diagnostic information derived from MR, especially if the adjunctive data were coregistered with the MR image volume and could be seamlessly acquired during the same procedure. This type of coregistered, complementary image data could improve the specificity of breast MR, allowing the diagnostic community to harness the substantial clinical benefits of the technique without also having to cope with the additional uncertainty it often generates.

Microwave tomography (MT) has been studied in simulation, phantom, and pilot clinical experiments for over 30 years.[17–19] Motivation arises primarily from the fact that the inherent dielectric properties of tissues can vary considerably, and when they deviate from their normal range they can become biomarkers of various pathologies including cancer, ischemic heart tissue, leukemia, and bone degradation.[18,20–23] MT has the added benefit that microwave signals are nonionizing unlike x-ray computed tomography (CT), mammography, and positron emission tomography (PET).[24–26]

We have shown that MT has substantial diagnostic potential, especially in the discrimination of breast cancer from other benign abnormalities.[19] This study reported an AUC [area under the receiver operating characteristic (ROC) curve] as high as 0.89 for breast lesions larger than 1 cm[19] which is comparable to diagnostic outcomes for MR.[5] These results are due to the excellent specificity of the MT technique compared with superior sensitivity as in the case of MR.[27,28] Our MT data indicate that the proportional increase in (electrical) permittivity, which has been observed with increasing breast density,[20,29,30] also results in cancer and reflects higher water content in breast disease. However, the threshold change found in cancer (electrical) conductivity occurs because the amount of water in malignancy is sufficient to saturate its local binding sites leading to an increase in unbound water in cancer that is not evident in either dense normal parenchyma or other benign processes in the breast. The bound water fraction in breast cancers has also been studied *in vivo* with optical spectroscopy[31,32] and these results are consistent with our MT findings that breast cancers have a higher fraction of free water—i.e., lower bound water index, BWI (which is largely responsible for the considerable conductivity contrast we observed in tumors with MT). Interestingly, the optical measurements were shown to be directly proportional to the apparent diffusion coefficient (ADC) in phantoms,[33] but the *in vivo* results contradict other ADC measurements in breast cancer—the latter indicating that water mobility in tumors is decreased relative to benign lesions and normal breast parenchyma.[34] The low water mobility reported with diffusion-weighted (DW) MRI may be related to the number of macromolecules and cellular membranes in breast cancers which can compromise local measurements of bound vs free water with DW-MRI (because these constituents represent potential barriers to free water diffusion). While the exact mechanisms involved (which would explain the differences in the bound water optical, and similarly our MT, results, and ADC DW-MRI measurements in breast cancers) are unclear, MT permittivity and conductivity (like the optical results) appear to be sensitive to different attributes of the tumor microenvironment which govern bound-free water fraction and ionic flow relative to MRI parameters (such as ADC); and thus, offer the potential of new complementary information for breast cancer diagnosis that could improve the specificity of breast MR.

At microwave frequencies above a few GHz, the dielectric properties of tissue water, be it bound or free, are effectively the same as bulk water;[35] however, tissue water behaves differently at lower microwave and UHF frequencies, and whether it is free or bound is critical in determining its observed dielectric properties. For example, studies have shown that while permittivity follows a typical Maxwell-Fricke mixture law fairly closely in terms of water content at lower frequencies, conductivity exhibits a deviation that is directly related to bound water fraction.[36,37] In effect, tissue conductivity cannot increase appreciably until sufficient free water is available for the free flow of ions, and bound water does not offer this environment. Rather, bound water has its own relaxation frequency ranging between 0.1 and 1 GHz depending on the degree of binding.[35] An additional tissue relaxation process, termed *UHF relaxation*,[38] which operates primarily in the UHF and lower microwave frequency range, has the net effect of substantially decreasing the conductivity of tissue in the low GHz region.[23] Thus, while permittivity increases almost linearly with increased overall water content in this spectral span, conductivity remains low until high overall water content is reached, allowing the conductivity of tissue with high amounts of bound water (e.g., fibroglandular tissue) to be low, but tumor conductivity to be high because of a much larger proportion of free water. While these formative studies were performed primarily in muscle where the amount of bound water was estimated to be equivalent to 0.4–0.6 g of water per gram of protein, fibroglandular breast tissue is comprised largely of hyaluronic acid which has been called a "sponge" because of the way it binds water.[39] Hence, one would expect the free/bound water effect to be even more pronounced in fibroglandular breast tissue than in muscle given that the hyaluronic acid in the former is known to bind as much as 0.7–1.0 g of water per each gram of sugar.[40]

Interestingly, the phenomenon was not observed in the dielectric property studies of Lazebnik *et al.*;[20,41] however, this characteristic of tissue conductivity is apparent at frequencies below 2.5 GHz where the bound water effects and UHF relaxation are known to influence the dielectric properties.[35,36,38] Further, the Lazebnik reports applied a single Cole-Cole relaxation over the analysis bandwidth (0.5–20 GHz) whereas studies[38] indicate that a substantial deviation occurs in tissue dielectric properties from a single Cole-Cole curve around 2.0–2.5 GHz—the implication being that bound/free water differentiation is only observable at the lower frequencies. Thus, these tissue conductivity behaviors may have been overlooked in the Lazebnik data because a single Cole-Cole relaxation was applied, and the conductivity values of tissue

are often two orders of magnitude less than those at higher frequencies (which then dominated the single dispersion fit, and missed this potentially important and promising contrast regime).

Unfortunately, the spatial resolution of MT is relatively poor and detection of sharp transitions in microwave properties is blurred substantially by the regularization that is required to stabilize MT image reconstruction. Thus, the diagnostic potential that appears to be available in the intrinsic microwave property characteristics of normal, abnormal benign, and malignant breast tissue have not been fully realized. Consistently with other diffuse imaging technologies when combined with MR,[42] we have found that the spatial scale on which microwave properties can be accurately recovered is substantially improved when anatomical information from MR is included.[43,44] As a result, we have pursued a new combined imaging technology, termed Magnetic Resonance Microwave Tomography (MRMT).

Concurrent combination breast imaging in the diagnostic/screening setting has been dominated by the addition of optical methods to conventional modalities, for example, to x-rays,[45–47] ultrasound,[48,49] and MR;[42,50] most likely because optical technologies offer the potential of molecular specificity that can be integrated with clinically accepted breast imaging methods at moderate cost. We have experience at Dartmouth with multimodality combinations involving diffuse light in the near-infrared, termed Near InfraRed Spectral Tomography (NIRST), and have developed platforms with breast x-ray tomosynthesis[51,52] and MR.[53,54] Similar to MT, NIRST alone provides molecular specificity in terms of intrinsic breast tissue composition, but at poor spatial resolution, and when used in combination is significantly advantaged by the high-resolution spatial information provided by traditional breast imaging. The most robust and diagnostically significant NIRST parameter has been total hemoglobin concentration, Hb_T, evidently because it is a surrogate for localized vascular density and associated angiogenic activity in cancers.[19,55] In prior studies,[29] MT conductivity has been highly correlated with NIRST Hb_T in the breasts of women examined with both modalities, and hence, the addition of MR spatial information should similarly strengthen the diagnostic accuracy of MT. Further, MT offers some potential advantages over NIRST—namely, its noncontacting imaging array (eliminating poor/inconsistent sensor contact effects, albeit a coupling fluid is involved), and its much higher frequency signal amplitude and phase for image reconstruction (NIRST light is amplitude-modulated around 100 MHz to generate the detected signal amplitude and phase response) with much less signal attenuation (NIRST attenuation is also dependent on the source wavelengths of light). Whether MRMT proves to outperform its MR-NIRST analog, or some other multimodality breast imaging combination remains to be seen, but at minimum, a robust MRMT breast imaging platform must first be developed before any quantitative (data-driven) comparisons can occur.

Accordingly, in this paper we present the first combination of MT with MR in the clinical setting of breast imaging. While related efforts are currently underway to image the breast serially with MR and microwaves by fixing the breast in a thermoplastic mold[56] to allow for comparison and coregistration of the MR and microwave image data, this effort has not yet been realized in a clinical form. In our implementation, the subject undergoes a standard contrast-enhanced breast MRI exam simultaneously with the MT data acquisition, and suspicious regions identified by the MR contrast enhancement are segmented and integrated into a soft prior image reconstruction technique summarized below.[44] Here, we have strategically reduced the size of the MT imaging array and associated coupling fluid to accommodate variable breast sizes even within the MR scanner bore. In addition, the nonmagnetic monopole antennas with their low-profile design function effectively in the MR environment because they cause modest (and acceptable) MR image distortions in the breast volume of interest. The radiofrequency (RF) gradients applied during MR sequences produce high power signal bursts that can saturate and desensitize the MT receivers, and subsequently disrupt the electromagnetic (EM) signals of interest. We discuss these compatibility issues and demonstrate strategies to minimize signal corruption through hardware modifications which are subsequently validated through phantom experiments. Finally, we present some of the first examples of MT image recovery where spatial information from MR images has been encoded via our soft prior regularization scheme[44] to produce accurate estimates of the microwave properties of internal features identified through MR.[57]

2. METHODS

In this section, we describe the current MR and MT systems and their integration. Descriptions include a summary of our microwave tomography technique, the MR scanner specifications, and the basic layout of the MT data acquisition hardware, illumination tank, and associated cabling. We discuss the MT antenna configuration and considerations for minimizing its impact on the MR images. We also present strategies implemented for minimizing MT multipath signals in the confined, near-field radiation zone of the antenna array when placed in the bore of the MR scanner and analyze effects of the MR RF gradients on the MT signals of interest. Finally, we summarize modifications to our MT image reconstruction methods which exploit the coregistered anatomical information available from the MR image volume.

2.A. Microwave tomography

Microwave tomography is analogous to classical x-ray tomography in that a target of interest (i.e., the breast) is illuminated sequentially with antennas surrounding the tissue, and the associated scattered signals resulting from each illumination are measured by the remaining antennas constituting the imaging array. In the case of our imaging system, the breast is pendant in a coupling liquid comprised of glycerin and water that includes an array of monopole antennas. The lossy nature of the liquid minimizes multipath contributions arising from unwanted signal reflections off the tank walls and base, dampens mutual coupling artifacts between adjacent antennas, and

provides an appropriate impedance match to minimize signal attenuation from reflections at the breast/liquid surface. We utilize a Gauss-Newton iterative algorithm to reconstruct microwave property images (i.e., electrical permittivity and conductivity) which has been shown to produce both 2D and 3D images[30,58] from data acquired during clinical breast exams. This technique turns image reconstruction into a parameter estimation problem that seeks to minimize the differences between measured and computed electric field values written as

$$\min \|E^m - E^c(k^2)\|^2, \tag{1}$$

where E^m and E^c are the measured and computed field values, respectively, and k^2 is the wavenumber squared which is comprised of the dielectric properties—in this case the permittivity (ε) and conductivity (σ)—within the target region. During minimization, the k^2 distribution is updated at each iteration through solution of the field problem to generate E^c based on the current estimate of the microwave property distribution (i.e., k^2). The process terminates once the L_2 norm of the residual has reached a minimum. Unlike x-ray CT, the microwave signals are highly scattered by the intervening tissue which contributes to the imaging problem being nonlinear and ill-posed. To address these issues, we have exploited a classical Box-Cox transformation which stabilizes the data variance and produces a more normal distribution of the problem residual.[59] In this case, we apply the log transformation which modifies the minimization statement in Eq. (1) to produce

$$\min \|\Gamma^m - \Gamma^c(k^2)\|^2 + \|\Phi^m - \Phi^c(k^2)\|^2, \tag{2}$$

where Γ and Φ are the log amplitude and phase of the electric fields in Eq. (1), respectively. The process has enabled us to reconstruct images without the typical limitations in microwave tomography such as instability and convergence to local minima.[60] To the best of our knowledge, only a few groups, including ours, have adopted this technique and are able to reconstruct images directly from the data without introducing prior information on the property values, themselves.[61,62] The algorithm is applicable to both 2D and 3D problems and is readily integrated with spatial priors,[43,44] as described in more detail below (in Sec. 2.E). It has also been applied with other minimization techniques such as contrast source inversion.[61] More details about the algorithm are available in earlier works.[63–67]

2.B. MR and MT system configurations

The MR scanner was a Philips Achieva (X-series) 3T unit which provided eight acquisition channels and imposed gradient strengths up to 80 mT/m. Software release R2.6.3.7 was installed on the system at time of the phantom and human subject studies described here. The Philips breast software package (release 2061) was also available and two circular flex coils [Sense Flex Medium IPX4, Philips Healthcare; see Figs. 1(b) and 9] were placed around the breast during clinical exams in lieu of a more conventional breast coil platform

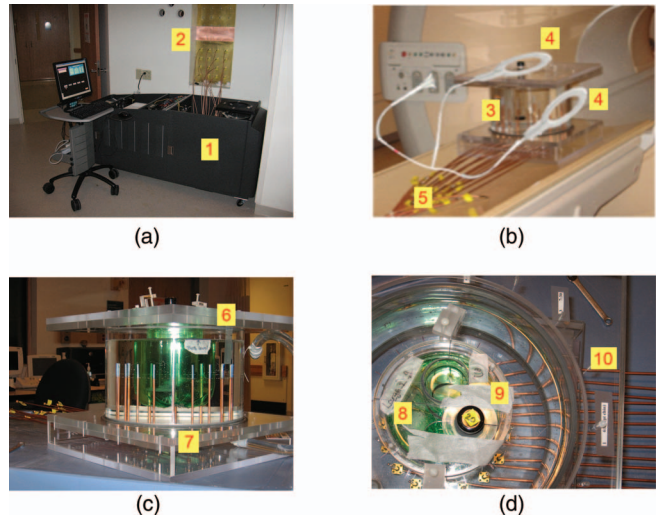

FIG. 1. Photographs of (a) the MT data acquisition system (1) in the MR control room with feedline cables attached to the SMA mounted bulkhead penetration panel (2), (b) the MR-compatible imaging tank (3) with mounted flex coils (4) and semirigid cables extending from the MT antenna array (5), (c) side view of the imaging tank with a breast phantom (6) surrounded by the MT antenna array (7), and (d) a top-down view of the imaging tank with a phantom having large (8) and small (9) inclusions showing cables (10) attached to flange connectors in the tank base.

which was replaced by the MT antenna array and associated fluid coupling tank.

MT system electronics were positioned outside the scanner bay by running long, flexible coaxial cables from the antenna array in the MR bore to 16 SMA flange connectors located on a custom penetration panel between the exam and external control rooms. Figure 1(a) shows our dedicated, standalone breast imaging system positioned next to the MR penetration panel (on the control room side) with short coaxial cables connecting its transceiver modules to the panel bulkhead. While the longer feedlines to the active antennas in the array add considerable signal loss (7.9 dB return path attenuation at 1.5 GHz for the 6.5 m cables—LMR200 from Times Microwave Systems, Wallingford, CT), they did allow us to connect a MR-compatible MT tank/antenna array with our standalone electronics system docked in the MR control room. Lower loss cables are available (e.g., LMR600—2.0 dB loss at 1.5 GHz for the return path loss over 6.5 m long cables) and will be implemented in the future, which will allow MT operation at higher excitation frequencies (e.g., up to 2.5 GHz, since signal losses in the MT imaging tank increase considerably with frequency). Similar to our dedicated MT breast imaging array when used standalone, the monopole antennas were configured on a 15.2 cm diameter circle and each antenna was operational in either transmit or receive modes. For each image, we collected 240 measurements (16 transmitter × 15 receivers) at discrete frequencies from 700 to 1700 MHz in 200 MHz increments.

2.C. MR image artifact reduction

An important consideration in combining MT with MR is reduction of MR image artifacts caused by the presence of

FIG. 2. Photographs of (a) a reduced-height tank with breast phantom (green) and monopole antennas with straight, 5.0 cm (short) feedlines, and (b) antenna array with 9.0 cm serpentine feedlines (tank wall removed).

the MT array. Toward this end, we minimized metal content in the MT array whenever possible. For example, the connections leading directly away from the illumination tank were replaced with 3.58 mm diameter, semirigid coaxial cables consisting of a copper outer conductor and a silver-plated, copper center conductor as shown in Fig. 1(b). Once these connections were extended more than 1 m from the MT imaging tank, they were transitioned to flexible coaxial lines which were far more convenient and practical for the long spans from the scanner to the penetration panel interface. Phantom studies were performed to evaluate the EM compatibility of connectors, cables, and other MT array components by assessing their effects on the MR image. Figure 1(c) shows a typical 19 cm height × 26.0 cm diameter phantom experiment involving the MT tank used to assess MR image quality. Figure 1(d) presents a top-down view which shows the monopole antennas and associated copper-clad, semirigid coaxial feed lines, and flange connectors on the under surface of the tank (the coaxial cables consisted of a 1.16 mm diameter center conductor, a 3.05 mm insulator diameter, and 3.58 mm outer conductor diameter).

2.D. MT multipath signal attenuation

Multipath signals are especially challenging in the near-field of antenna arrays when little opportunity exists for natural physical isolation of transmitters and receivers. Utilization of a lossy coupling fluid is very effective in reducing multipath effects. For example, in earlier work, we determined that the tank side walls could be placed as close as 7 cm from the antennas without reflections (from the walls) interfering with the transmission signals of interest.[68] In addition, we found that the tips of the monopole antennas could be placed as close as 2 mm from the air-liquid interface without inducing major artifacts in the MT images.[68] However, our standalone antenna arrays were housed in relatively deep tanks (typically 24–30 cm in depth) which did not appear to promote multipath signals. Since space is a premium in the MR bore, we initially reduced the MT tank height to 8.0 cm with shorter, straight antenna feedlines [Fig. 2(a)]. As described in more detail elsewhere,[69] this configuration generated multipath signals resulting from surface wave propagation (down and up the outside of the coaxial feedlines) along the tank base/liquid interface. A minimum feedline length of 9.0 cm in the lossy liquid was found to attenuate these surface currents to a level comparable to our deeper standalone MT antenna chamber. We retained the shorter 8.0 cm height tank (required for use in the MR bore) by precision bending the semirigid coaxial lines into a serpentine shape as shown in Fig. 2(b).

2.E. MT image reconstruction: Soft prior regularization

We adapted our log-transformed Gauss-Newton iterative reconstruction algorithm[64] with a regularization process which penalizes the weightings between two pixels in different predetermined regions of the imaging field-of-view, but rewards property uniformity for pixels within the same region. The predetermined or prior regions were created through MR segmentation of the anatomical structures of interest, for example, the adipose and fibroglandular tissues in the breast. The details can be understood more clearly in the following equation:

$$J^T J\{\Delta k^2\} = J^T \begin{Bmatrix} \Gamma^m - \Gamma^c(k^2) \\ \Phi^m - \Phi^c(k^2) \end{Bmatrix} + \lambda L\{k^2 - k_o^2\}, \tag{3}$$

which is used to calculate the updates to the image (Δk^2) during the iterative process where J is the Jacobian matrix, T designates matrix transpose, λ is the regularization parameter, and the subscript o designates the starting value of k^2. The soft prior matrix, L, encodes the spatial information and is implemented for a simple two region case as

$$L = \begin{bmatrix} \begin{matrix} 1 & -1/N_1 & -1/N_1 & -1/N_1 \\ -1/N_1 & 1 & -1/N_1 & -1/N_1 \\ -1/N_1 & -1/N_1 & 1 & -1/N_1 \\ -1/N_1 & -1/N_1 & -1/N_1 & 1 \end{matrix} & 0 \\ 0 & \begin{matrix} 1 & -1/N_2 & -1/N_2 & -1/N_2 & -1/N_2 & -1/N_2 \\ -1/N_2 & 1 & -1/N_2 & -1/N_2 & -1/N_2 & -1/N_2 \\ -1/N_2 & -1/N_2 & 1 & -1/N_2 & -1/N_2 & -1/N_2 \\ -1/N_2 & -1/N_2 & -1/N_2 & 1 & -1/N_2 & -1/N_2 \\ -1/N_2 & -1/N_2 & -1/N_2 & -1/N_2 & 1 & -1/N_2 \\ -1/N_2 & -1/N_2 & -1/N_2 & -1/N_2 & -1/N_2 & 1 \end{matrix} \end{bmatrix},$$

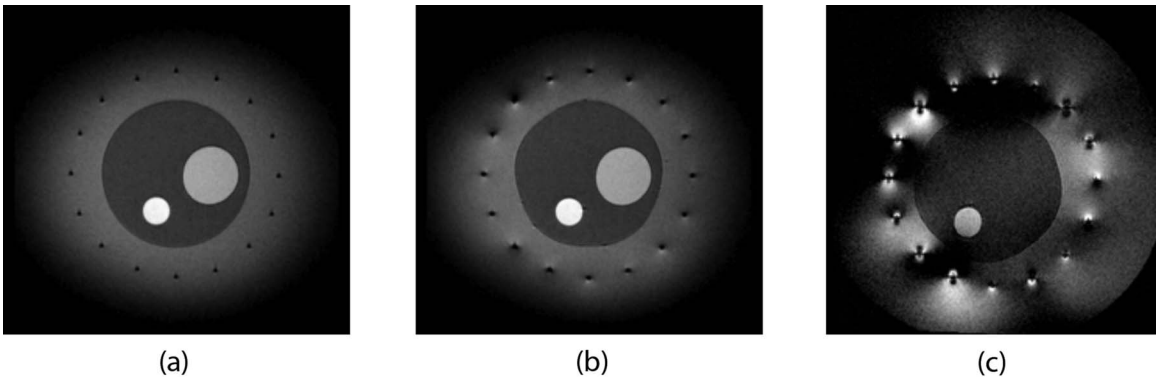

FIG. 3. T_2-weighted MR images of the MT imaging tank containing a 10.8 cm circular phantom with 4.2 and 2.0 cm inclusions: (a) MR image in the center plane of the active antennas, (b) MR image in a plane 3 cm below the interface between the semirigid coaxial line and the antenna. In (a) and (b), the coaxial line center conductors feeding the MT array were silver-plated copper. (c) MR image at the center plane of the monopole antennas for the same 10.8 cm circular phantom with the 2.0 cm inclusion when the coaxial cable center conductors were steel.

where N_1 and N_2 are the number of nodes within each of the two predefined regions of the reconstruction mesh. This can be easily generalized to an arbitrary number of regions. In effect, the regularization prefers image reconstruction solutions with property uniformity in the segmented zones but does not constrain the properties to be constant; that is, property variation within zones that is consistent with the generation of model responses which match the measurement data is allowed (hence, the soft prior nomenclature). The resulting image reconstruction algorithm has proved to be robust, is not sensitive to initial property distribution estimates (we use coupling fluid values as the starting point for each region), and does not suffer from convergence to local minima.[60] Computational details and performance characterization of the method have been reported.[44]

2.F. Region identification, segmentation, and mesh generation

Effective encoding of spatial priors in microwave image reconstruction requires software tools for region identification, segmentation, and mesh generation. In this study, we identified two tissue types—adipose and fibroglandular tissue—and they were assumed, individually, to be of similar electrical properties during the soft prior reconstruction. We used an inhouse MATLAB (Mathworks, Natick, MA) graphical user interface (GUI) to segment the regions of interest in the appropriate MR image cross-section of the breast (or phantom). For the MR image and soft prior mesh created from the breast exam described in Sec. 3.D [Figs. 10(b) and 10(c)], the 2D triangular-element reconstruction mesh was comprised of 2473 nodes and 4647 elements. In order to capture the irregular tissue geometry appropriately, the GUI controls the nodal sampling density and deploys a sufficient number of nodes on the boundaries of adjacent regions so that the interfaces between predefined (spatial prior) zones in the reconstructed image are smooth.

3. RESULTS

In this section, we present results on MR image artifacts, MT amplifier desensitization, and phantom and breast images from our combined MRMT system.

3.A. MR image artifacts from MT

Figure 3 shows T_2-weighted (T2W) MR images of a 10.8 cm diameter cylindrical breast phantom (84:16 glycerin/water) with 4.2 and 2.0 cm diameter cylindrical inclusions filled with 72% and 55% glycerin mixtures, respectively. The MR imaging sequence consisted of T2W TSE (turbo spin echo) with TR = 3000 ms, TE = 160 ms, and slice thickness = 3 mm. The first imaging plane (a) transects the monopole antennas while the second (b) intersects the coaxial feedlines 3 cm below the exposed dielectric which marks the antenna-feedline interface. Figures 3(a) and 3(b) present MR images acquired when cables with silver-plated copper center conductors were used. For the tissue imaging plane in (a), minor artifacts are evident around the surrounding antennas, but these distortions do not impact the phantom image quality which has a MR signal-to-noise ratio of 41 dB. In fact, the positions of the antennas are accurately marked for coregistration of the MT array geometry relative to the tissue of interest. At the lower plane transecting the feedline in (b), the artifacts have increased and perturbations in the shape of the phantom and its inclusions are evident but the MR SNR remains high at 43 dB. The MR image in Fig. 3(c) of the same phantom (with only the smaller inclusion) were acquired in the same plane as Fig. 3(a), but with coaxial lines having steel center conductors dropping the SNR to 4 dB which demonstrates the importance of maximizing the MR compatibility of the MT antenna array.

3.B. MT signal corruption from MR

The RF pulses from the MR system occur primarily at the Larmor frequency (128 MHz for the 3T system used here). Indeed, measurements through the antenna with an Agilent E4402B Spectrum Analyzer (SA) indicated high signal

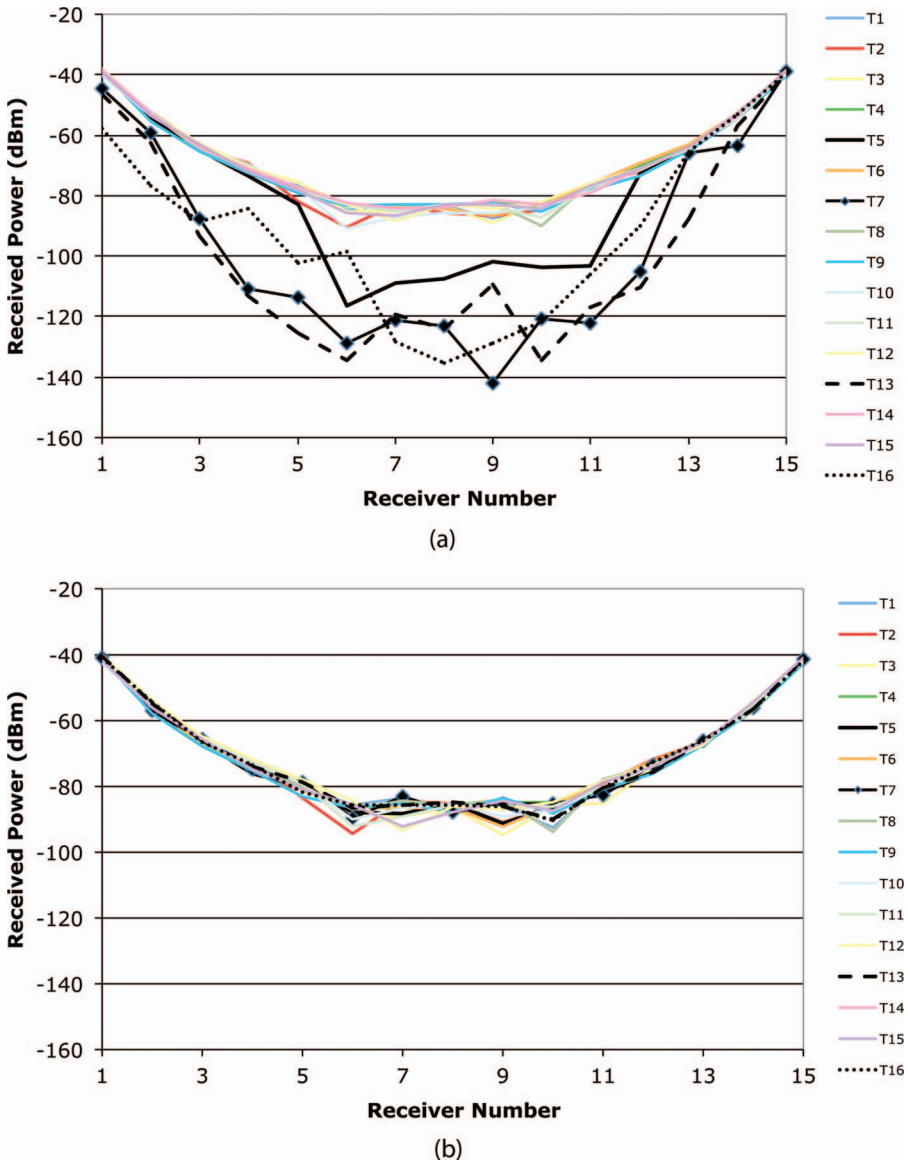

FIG. 4. Measured 1300 MHz MT signal amplitudes as a function of receiver number for all 16 transmitting antennas when the imaging tank is placed in the MR bore and MR data are acquired with (a) no high pass filters, and (b) two high pass filters installed in the MT measurement channels, respectively. The distorted curves (transmitters 5, 7, 13, and 16) are those which extend below the −80 dBm level in (a).

levels at the Larmor frequency and its harmonics. These data were measured with the antenna array submerged in an 80% glycerin coupling bath and the acquired signals transmitted through the long coaxial cables and connector bulkhead to the SA. Despite the fluid bath attenuation (which does drop substantially at frequencies as low as the Larmor fundamental frequency) and the relatively poor coupling efficiency to the antenna, the power levels measured for the Larmor fundamental and first six harmonics (128, 255, 383, 510, 638, 766, and 893 MHz, respectively) were nominally 0, −40, −50, −67, −72, −77, and −79 dBm, respectively. Because of the transient nature of the RF pulses, these power levels were estimates based on visual observations of the SA during continuous operation of the MR scanner.

Figure 4(a) shows plots of the measured MT signal amplitudes (uncalibrated) at 1300 MHz for 15 receivers collecting data from all 16 transmitters delivering 1 mW (0 dBm) of power. Many of the data traces exhibit the typical pattern for received signals, i.e., a symmetric parabolic distribution with the minimum signal occurring at the receiver directly opposite the transmitter in the circular antenna array. (Note that there are minor variations between the curves due to the fact that the gains of the different receive and transmit channels are not identical. Given that these are uncalibrated data sets, we would not expect perfect alignment, but the overall trends are instructive.) However, the power levels for the four corrupted sets (transmitters 5, 7, 13, and 16) are 20–40 dB lower than those received from the other transmitters. Because the MR RF pulses are intermittent and not synchronized with the MT data acquisition, the distortions did not affect all transmissions. Had the signal distortions been from simple constructive (or destructive) addition of one of the Larmor harmonics

with the transmitted signals of interest, positive and negative perturbations around the predicted pattern would have been visible mostly at the lower signal levels. This would have been a more predictable corruption mechanism. Instead, the distortions evident in Fig. 4(a) appear to be the result of amplifier desensitization, whereby corrupting signals are processed simultaneously with those of interest and have sufficiently high amplitude to saturate the small signal amplification required for the signal of interest. Given that the measured signal leakage from the fundamental Larmor frequency was 0 dBm after being picked up by an antenna, it easily saturates the first stage of 20 dB of receiver amplification (subsequent cascaded amplifier gain elements are even more saturated). After installing two VHF-740 Mini-Circuits high pass filters (combined attenuation of 122 dB at 128 MHz), the distortions appearing transiently in Fig. 4(a) completely disappear as shown in Fig. 4(b).

3.C. Phantom imaging experiments

During the initial stages of MRMT system development, we completed a number of phantom experiments where the MT data were collected both inside the MR bore during (MR) scanning and outside the MR bore (in the MR control room) as a data quality check on the fully integrated MRMT hardware. These experiments were cumbersome and lengthy to perform because we had to assemble/disassemble the long cable connections from the custom penetration panel to the phantom-bearing intrabore MT antenna array as well as the short cable connections from the MT data acquisition hardware to the penetration panel, and reassemble all of these connections when the phantom-bearing MT array was relocated (from the scanner bore) to the MR control room. Figure 5 shows a representative pair of permittivity images based on intra- and extra-bore MT data obtained from the same type of three-region, two-inclusion phantom described in more detail below, which demonstrate that the image recovery from the two MT data sets (intra and extra-bore) is very similar. Here, the corresponding conductivity images are not presented because they did not localize the inclusions in either case. Improvements in our hardware and experimental procedures (e.g., we moved from the high to low profile tank/curved antenna array; see Fig. 1 vs Fig. 2) subsequently led to successful recovery of conductivity images (e.g., in Fig. 7), but we did not return to these types of intra/extra-bore experiments because of their logistical complexities.

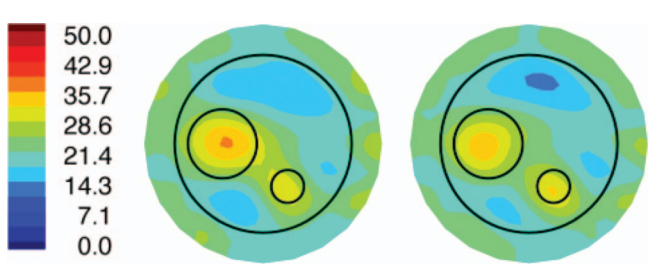

FIG. 5. MT (relative) permittivity images (at 1100 MHz) of a breast-sized phantom (outer circle) with fibroglandular (large circle) and tumor (small circle) inclusions reconstructed from data acquired with the MT antenna array located outside (left) and inside (right) the bore of the MR scanner. Color scale (left) is shown.

We then performed full intrabore MRMT phantom experiments with simultaneous MR and MT data acquisition. The MR sequence was a T_2-weighted TSE with acquisition parameters TR = 3000 ms, TE = 160 ms, and slice thickness = 3 mm. These microwave images were reconstructed from data recorded at 1300 MHz (vs 1100 MHz in Fig. 5). The tank was filled with a solution of 80% glycerin (20% tap water) having measured dielectric properties of $\varepsilon_r = 20.9$ and $\sigma = 1.22$ S/m, respectively. A 10.8 cm diameter tube representing an approximate breast cross-section was filled with an 84% solution of glycerin (16% water) and 4.2 and 2.0 cm diameter offset cylindrical regions were placed inside and consisted of 72% and 55% glycerin:water mixtures. The properties of the three regions were $\varepsilon_r = 16.1$ and $\sigma = 1.03$ S/m, $\varepsilon_r = 30.2$ and $\sigma = 1.51$ S/m, and $\varepsilon_r = 51.2$ and $\sigma = 1.44$ S/m, respectively. The three regions were nominally intended to mimic the properties of a fatty breast, fibroglandular tissue and tumor, although the corresponding electrical conductivities were larger than expected for this composition (especially for fat). Figure 3(a) shows the corresponding T_2-weighted MR image of the horizontal plane through the phantom and the center of the active section of the antenna array. The location of the phantom and associated inclusions with respect to the individual antenna positions is clearly evident. Figure 6(a) shows the uniform 14.5 cm diameter reconstruction mesh comprised of 559 nodes and 1044 triangular elements while Fig. 6(b) contains the soft prior reconstruction mesh containing 1034 nodes and 1821 elements discretized from the MR image.

Figures 7(a) and 7(b) present the recovered 1300 MHz permittivity and conductivity images of the phantom using our standard Tikhonov regularization and the soft-prior regularization that exploits the MR-derived prior information. In Fig. 7(a), the phantom and its inclusions are visible in the permittivity image reconstructed with the standard (no priors) MT approach but with some artifacts. Well-defined inclusions are less visible in the conductivity image, in part because of the reduced property contrast in the constituent liquids. Circles are drawn over the MT images to indicate the exact locations of the phantom and inclusions. The average property values recovered in the two inclusions were 25.1 and 1.27 S/m, and 29.1 and 1.25 S/m, respectively, which are considerably lower than the actual values. For the soft prior images in Fig. 7(b), the average values in the phantom background and inclusions are $\varepsilon_r = 16.7$ and $\sigma = 1.03$ S/m for the 10.8 cm cylinder, $\varepsilon_r = 28.6$ and $\sigma = 1.41$ S/m for the 4.2 cm cylinder, $\varepsilon_r = 47.3$ and $\sigma = 1.27$ S/m for the 2.0 cm cylinder, respectively. These values are closer to the actual properties (6% and 9% average error in permittivity and conductivity, respectively, relative to 30% and 16% without priors) and demonstrate that the soft prior technique is quantitatively more accurate than the standalone approach. Figures 8(a) and 8(b) present transects through the inclusions in the soft-prior MRMT images further demonstrating the high quality of the recovered properties.

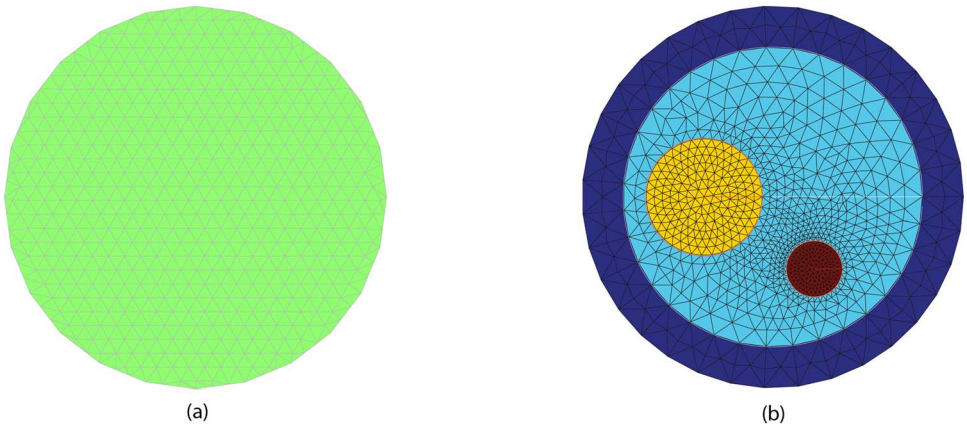

FIG. 6. MT image reconstruction meshes: (a) uniform, with 559 nodes and 1044 elements, and (b) soft prior-based with 1034 nodes and 1821 elements, respectively.

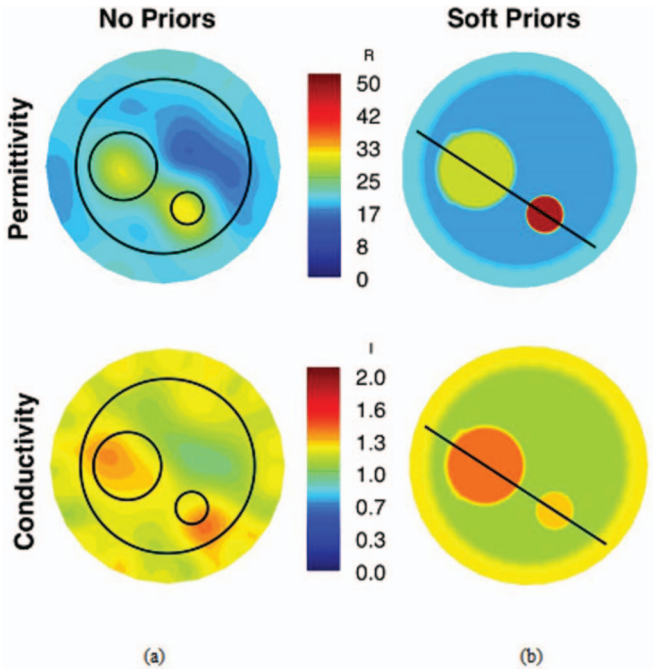

FIG. 7. Reconstructed 1300 MHz permittivity and conductivity images of the three-region phantom (circles indicate object locations) from (a) standard Tikhonov and (b) MR-derived soft prior regularization. Recovered property profiles along the transect lines through the inclusions are shown in Fig. 8.

3.D. Breast images

We imaged a 43 year old woman in our combined MRMT system under an IRB-approved experimental protocol with informed consent. The subject had heterogeneously dense breasts, a body mass index of 25, and no known breast abnormalities. The MR exam consisted of axial T_1 images with TR = 82.9 ms, TE = 10 ms, and slice thickness = 3 mm, using two circular flex coils, as shown in Fig. 9. The MT data were acquired over a frequency range of 900–1700 MHz in increments of 200 MHz.

Figure 10(a) shows the subject positioned prone on the MR table with the MT platform located below. Figure 10(b) presents an anatomically coronal T_1-weighted MR image at the midplane of the active section of the MT antenna array. In this geometry, the monopole antennas were oriented vertically (and perpendicularly) to the horizontal MR-image plane. They appear as the black/white artifacts uniformly positioned around the breast in Fig. 10(b) cross-section. Because both the antennas and breast are visible in the MR image, coregistration of the two for soft prior spatial encoding is automatic. MR image SNR of the relatively uniform fat was 13 dB. Figure 10(c) contains the soft prior mesh created from a MATLAB (Mathworks, Natick, MA) GUI to discretize the segmented subregion boundaries from which a triangular mesh was generated. For the fibroglandular tissue, three

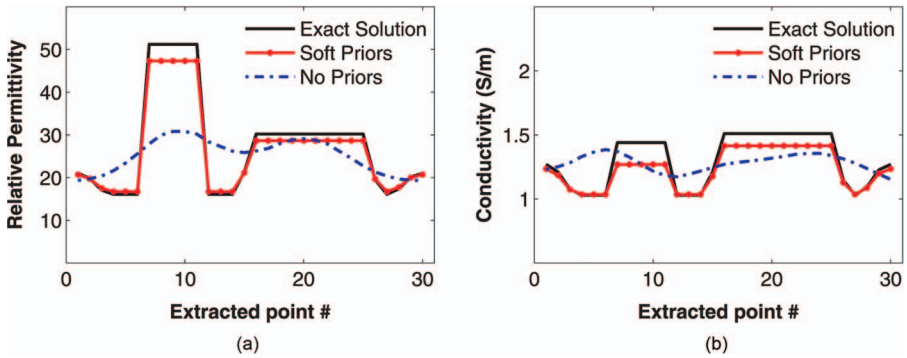

FIG. 8. Property profiles recovered along the transect lines shown in Fig. 7 for (a) permittivity and (b) conductivity, respectively, when MR-derived soft priors are applied compared with the exact values.

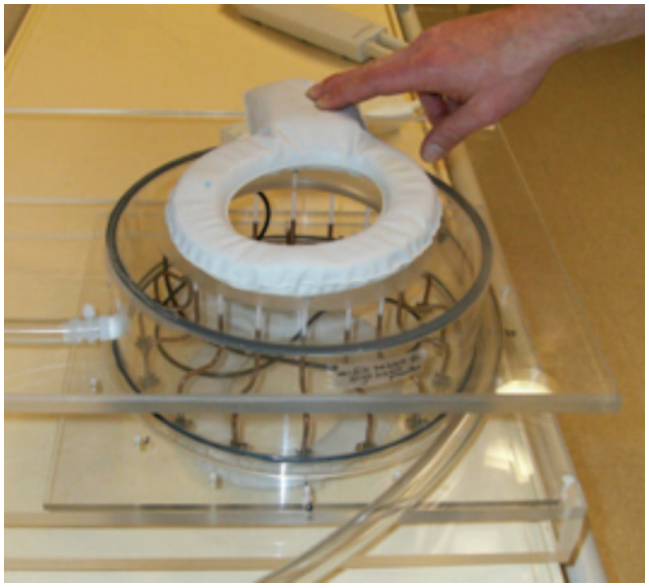

FIG. 9. Photograph of the flex coils used during the clinical exam positioned on the MRMT imaging tank.

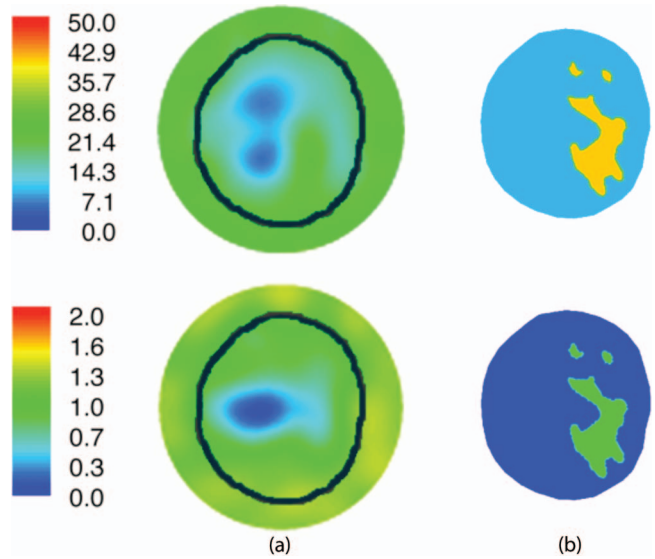

FIG. 11. Reconstructed 1300 MHz permittivity and conductivity images of the subject's left breast utilizing (a) standard Tikhonov and (b) soft prior regularizations, respectively. The known boundary of the breast (black contour) is overlaid on the no-prior (left) MT images for reference.

discrete zones (one larger and two smaller) were identified but were assumed to be of similar electrical properties during the soft prior MT image reconstruction.

The mesh was comprised of 2473 nodes and 4647 elements. Figures 11(a) and 11(b) show the 1300 MHz reconstructed images from the standalone MT (no priors) and MRMT (soft prior) regularization schemes, respectively. In the former, the breast perimeter is discernible in both permittivity and conductivity along with evidence of the general fat-fibroglandular structure of the internal parenchyma. The soft-prior MRMT images are essentially homogeneous for the fatty and fibroglandular tissue segmentations from MR. The recovered values are comparable to published *ex vivo* results for these tissue types.[20] Specifically, the MRMT adipose properties were $\varepsilon_r = 8.8$ and $\sigma = 0.09$ S/m, while those for fibroglandular tissue were $\varepsilon_r = 40.7$ and $\sigma = 0.96$ S/m, whereas the published values for these tissue types are $\varepsilon_r = 4.8$ and $\sigma = 0.05$ S/m for adipose, and $\varepsilon_r = 39.4$ and $\sigma = 0.75$ S/m for fibroglandular tissue, respectively (assuming 50% adipose content in the fibroglandular region).[20]

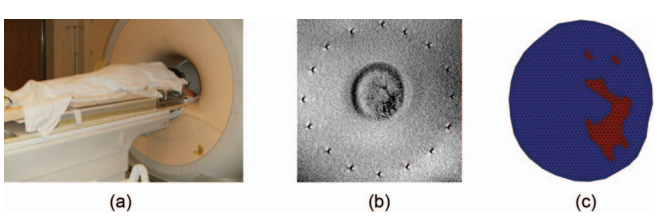

FIG. 10. (a) Photograph of a subject ready to undergo a MRMT breast exam. (b) Anatomically coronal T_1-weighted MR of the subject's left breast in the plane corresponding to the center of the active section of the MT antenna array. (c) Segmented soft prior mesh derived from the MR image in (b).

4. DISCUSSION

While serial MR and MT breast exams are possible, and steps can be taken to immobilize the breast during the two imaging studies (for example, by using a thermoplastic form molded to the specific breast shape of interest as is commonly used during radiotherapy)[56] to facilitate spatial registration of the image data, the additional exam time and the imperfect spatial and temporal relationships between the two imaging studies are impediments to the clinical evaluation/validation of combining MT and MR data for diagnostic decision-making. Thus, in this paper, we combine MT with MR as a coregistered multimodality breast imaging platform that exploits the fine spatial resolution of MR with the highly specific breast properties from MT. However, significant challenges exist when combining any technique with MR that are related to the physical size constraints and extreme electromagnetic environment inside the bore of the scanner. MT corruption of MR signal was minimized by reducing overall metal content and carefully selecting cable and connector composition. Proximity to the breast volume of interest is also important and sufficient image quality (MR SNR of 13 dB) was obtained, although further optimization is needed and custom-MR coil integration will likely be required to achieve diagnostic quality MR breast images in the future. Suppression of MT multipath signals that corrupt the data of interest has been maintained by preserving antenna array feedline length in the lossy coupling fluid, despite the reduction in tank height necessary to accommodate MR bore size limitations.

MR effects on the MT signal acquisition has also been investigated. Cascaded high-pass filters were added to each MT channel to eliminate contamination from the MR RF signals. While the Larmor frequency (128 MHz) is far from our MT operating frequencies, the relatively high power levels were found to desensitize the MT receiver front-end amplifiers and

effectively switched-off the small signal amplification that is necessary for effective MT imaging in tissue volumes comparable to the breast. Experiments demonstrated that once the signal from the fundamental Larmor frequency was rejected, high-quality MT data were acquired.

Phantom experiments are reported which show MT image reconstructions from data acquired inside the scanner bore are very similar to those recovered from the same phantom when the MT array was located outside the scanner bay. The first phantom images reconstructed from MT data collected simultaneously with MR imaging is also presented. The structural information from the MR scans was used to form a computational mesh of the imaging field-of-view for reconstruction of MT electrical permittivity and conductivity images. The improvement in property recovery in breast-sized phantoms with associated inclusions is dramatic. Specifically, in the larger inclusion the average electrical permittivity and conductivity errors are reduced from 17% to 5% and from 15% to 7%, respectively. Similarly, the corresponding errors in the smaller inclusion are reduced from 43% to 7% and from 13% to 12%. The accompanying breast images are also encouraging because they demonstrate that simultaneous collection of both MR and MT data is possible on a subject during a procedure that is similar to a standard MR exam. The resulting MT property images appear to be more accurate in terms of electrical permittivity and conductivity values for adipose and fibroglandular tissue when the structural information from MR is segmented into these dominant tissue types and corresponding regions within the breast.

While the MRMT breast imaging platform described here demonstrates the feasibility of acquiring MT data simultaneously with MR imaging, and the potential improvements in MT property accuracy gained by incorporating MR structural priors into the MT image reconstruction process, the approach still needs further investigation before it will be ready for clinical evaluation. Specifically, even though we have minimized the impact of the metal components of the MT antenna array (and associated connectors and cabling) on MR image quality, the breast images obtained during the human subject exam are not of sufficient diagnostic quality to be viable in practice. Our coil configuration was too far from the breast and not sufficiently integrated with the MT imaging tank to deliver the image quality required. A more fully integrated approach, for example, by embedding the MR breast imaging coils directly into the MT imaging tank, appears possible and is worth pursuing in the future. Additionally, the signal control, processing, and amplification for MR imaging could be integrated into the exam platform housing which would offer substantially improved performance.

5. CONCLUSION

Even though many levels of additional integration of MT with MR can be pursued in the future, the results presented here are encouraging. They represent the first demonstration of a simultaneous multimodality MRMT breast exam delivered to a human subject and indicate that MR priors are likely to substantially improve the accuracy of imaging electrical properties with MT data, which motivates pursuit of a fully integrated multimodality MRMT breast imaging platform.

ACKNOWLEDGMENTS

This work was supported by NIH/NCI grant # R33-CA102938 and the generous donations of Charlotte S. Metcalf and the Telaka Foundation.

[a]Author to whom correspondence should be addressed. Electronic mail: paul.meaney@dartmouth.edu

[1]M. D. Schnall, "Application of magnetic resonance imaging to early detection of breast cancer," Breast Cancer Res. **3**(1), 17–21 (2001).

[2]E. Warner, D. B. Plewes, R. S. Shumak, G. C. Catzavelos, L. S. Di Prospero, M. J. Yaffe, V. Goel, E. Ramsay, P. L. Chart, D. E. Cole, G. A. Taylor, M. Cutrara, T. H. Samuels, J. P. Murphy, J. M. Murphy, and S. A. Narod, "Comparison of breast magnetic resonance imaging, mammography, and ultrasound for surveillance of women at high risk for hereditary breast cancer," J. Clin. Oncol. **19**(15), 3524–3531 (2001).

[3]M. J. Stoutjesdijk, C. Boetes, G. J. Jager, L. Beex, P. Bult, J. H. Hendriks, R. J. Laheij, L. Massuger, L. E. van Die, T. Wobbes, and J. O. Barentsz, "Magnetic resonance imaging and mammography in women with a hereditary risk of breast cancer," J. Natl. Cancer Inst. **93**(14), 1095–1102 (2001).

[4]E. A. Morris, L. Liberman, D. J. Ballon, M. Robson, A. F. Abramson, A. Heerdt, and D. D. Dershaw, "MRI of occult breast carcinoma in a high-risk population," Am. J. Roentgenol. **181**(3), 619–626 (2003).

[5]D. A. Bluemke, C. A. Gatsonis, M. H. Chen, G. A. DeAngelis, N. DeBruhl, S. Harms, S. H. Heywang-Kobrunner, N. Hylton, C. K. Kuhl, C. Lehman, E. D. Pisano, P. Causer, S. J. Schnitt, S. F. Smazal, C. B. Stelling, P. T. Weatherall, and M. D. Schnall, "Magnetic resonance imaging of the breast prior to biopsy," JAMA **292**(22), 2735–2742 (2004).

[6]D. Saslow, C. Boetes, W. Burke, S. Harms, M. O. Leach, C. D. Lehman, E. Morris, E. Pisano, M. Schnall, S. Sener, R. A. Smith, E. Warner, M. Yaffe, K. S. Andrews, and C. A. Russell, "American Cancer Society guidelines for breast screening with MRI as an adjunct to mammography," Ca-Cancer J. Clin. **57**(2), 75–89 (2007).

[7]L. Esserman, E. Kaplan, S. Partridge, D. Tripathy, H. Rugo, J. Park, S. Hwang, H. Kuere, D. Sudilovsky, Y. Lu, and N. Jylton, "MRI phenotype is associated with response to doxorubicin and cyclophosphamide neoadjuvant chemotherapy in stage III breast cancer," Ann. Surg. Oncol. **8**, 549–559 (2001).

[8]S. G. Orel, "MR imaging of the breast," Magn. Reson. Imaging Clin. N. Am. **9**(2), 273–288 (2001).

[9]K. K. Lindfors, J. M. Boone, T. R. Nelson, K. Yang, A. L. C. Kwan, and D. W. F. Miller, "Dedicated breast CT: Initial clinical experience," Radiology **246**(3), 725–733 (2008).

[10]H. Chan, J. Wei, B. Sahiner, E. A. Raffert, T. Wu, M. A. Roubidoux, R. H. Moore, D. B. Kopanas, L. M. Hadjiiski, and M. A. Helvie, "Computer-aided detection system for breast masses on digital tomosynthesis mammograms: Preliminary experience," Radiology **237**(3), 1075–1080 (2005).

[11]S. P. Poplack, T. D. Tosteson, C. A. Kogel, and H. M. Nagy, "Digital breast tomosynthesis: Initial experience in 98 women with abnormal digital screening mammography," Am. J. Roentgenol. **189**, 616–623 (2007).

[12]S. G. Orel and M. D. Schnall, "MR imaging of the breast for the detection, diagnosis, and staging of breast cancer," Radiology **220**(1), 13–30 (2001).

[13]L. Bartella, C. S. Smith, D. D. Shaw, and L. Liberman, "Imaging breast cancer," Radiol. Clin. North Am. **45**, 45–67 (2007).

[14]V. F. Cocquyt, G. M. Villeirs, P. N. Blondeel, H. T. Depypere, M. M. Mortier, R. F. Serreyn, R. VanDen Broecke, and S. J. P. Van Belle, "Assessment of response to preoperative chemotherapy in patients with stage II and III breast cancer: The value of MRI," Breast J. **11**, 306–315 (2002).

[15]A. Rieber, H. J. Brambs, A. Gabelmann, V. Heilmann, R. Kreienberg, and T. Kuhn, "Breast MRI for monitoring response of primary breast cancer to neo-adjuvant chemotherapy," Eur. Radiol. **12**, 1711–1719 (2002).

[16]M. A. Parazella, "Gadolinium-contrast toxicity in patients with kidney disease: Nephrotoxicity and nephrogenic systemic fibrosis," Curr. Drug Saf. **3**, 67–75 (2008).

[17]J. C. Bolmey, A. Izadnegahdar, L. Jofre, C. H. Pichot, G. Peronnnet, and M. Solaimani, "Microwave diffraction tomography for biomedical applications," IEEE Trans. Microwave Theory Tech. **30**, 1998–2000 (1982).
[18]D. Colton and P. Monk, "A new approach to detecting leukemia using computational electromagnetics," IEEE Comput. Sci. Eng. **2**, 46–52 (1995).
[19]S. P. Poplack, T. D. Tosteson, W. A. Wells, B. W. Pogue, P. M. Meaney, A. Hartov, C. A. Kogel, S. Knowlton-Soho, J. J. Gibson, and K. D. Paulsen, "Electromagnetic breast imaging: Pilot result in women with abnormal mammography," Radiology **243**(2), 350–359 (2007).
[20]M. Lazebnik, D. Popovic, L. McCartney, C. B. Watkins, M. J. Lindstrom, J. Harter, S. Sewall, T. Ogilvie, A. Magliocco, T. M. Breslin, W. Temple, D. Mew, J. H. Booske, M. Okoniewski, and S. C. Hagness, "A large-scale study of the ultrawideband microwave dielectric properties of normal, benign and malignant breast tissues obtained from cancer surgeries," Phys. Med. Biol. **52**, 6093–6115 (2007).
[21]S. Y. Semenov, R. H. Svenson, A. E. Bulyshev, A. E. Souvorov, A. G. Nazarov, Y. E. Sizov, V. G. Posukh, A. Pavlovsky, P. N. Repin, A. N. Starostin, B. A. Voinov, M. Taran, G. P. Tatsis, and V. Y. Baranov, "Three-dimensional microwave tomography: Initial experimental imaging of animals," IEEE Trans. Biomed. Eng. **49**, 55–63 (2002).
[22]J. Sierpowska, "Electrical and dielectric characterization of trabecular bone quality," Ph.D. dissertation, Kuopio University, Kuopio, Finland, 2007.
[23]K. R. Foster and J. L. Schepps, "Dielectric properties of tumor and normal tissues at radio through microwave frequencies," J. Microwave Power **16**, 107–119 (1981).
[24]S. A. Feig and R. E. Hendrick, "Radiation risk from screening mammography of women aged 40-49 years," J. Natl. Cancer Inst. Monogr. **22**, 119–124 (1997).
[25]J. M. Boone, A. L. C. Kwan, T. R. Nelson, T. R. Nelson, N. Shah, G. Burkett, J. A. Seibert, K. K. Lindfors, and G. Roos, "Performance assessment of a pendant-geometry CT scanner for breast cancer detection," Proc. SPIE **5745**, 319–323 (2005).
[26]R. R. Raylman, S. Majewski, M. F. Smith, J. Proffitt, W. Hammond, A. Srinivasan, J. McKisson, V. Popov, A. Weisenberger, C. O. Judy, B. Kross, S. Ramasubramanian, L. E. Banta, P. E. Kinahan, and K. Champley, "The positron emission mammography/tomography breast imaging and biopsy system (PEM/PET): Design, construction and phantom-based measurements," Phys. Med. Biol. **53**, 637–653 (2008).
[27]S. Gabriel, R. W. Lau, and C. Gabriel, "The dielectric properties of biological tissues: III. Parametric models for the dielectric spectrum of tissues," Phys. Med. Biol. **41**, 2271–2293 (1996).
[28]K. R. Foster and H. Schwan, "Dielectric properties of tissues and biological materials: A critical review," Crit. Rev. Biomed. Eng. **17**(1), 25–104 (1989).
[29]S. P. Poplack, K. D. Paulsen, A. Hartov, P. M. Meaney, B. Pogue, T. Tosteson, M. Grove, S. Soho, and W. Wells, "Electromagnetic breast imaging: Average tissue property values in women with negative clinical findings," Radiology **231**, 571–580 (2004).
[30]P. M. Meaney, M. W. Fanning, T. Raynolds, C. J. Fox, Q. Fang, C. A. Kogel, S. P. Poplack, and K. D. Paulsen, "Initial clinical experience in microwave breast imaging in women with normal mammography," Acad. Radiol. **14**(2), 207–218 (2007).
[31]S. H. Chung, A. E. Cerussi, C. Klifa, H. M. Baek, O. Birgul, G. Gulsen, S. I. Merritt, D. Hsiang, and B. J. Tromberg, "*In vivo* water state measurements in breast cancer using broadband diffuse optical spectroscopy," Phys. Med. Biol. **53**, 6713–6727 (2008).
[32]S. H. Chung, H. Yu, M-Y Su, A. E. Cerussi, and B. J. Tromberg, "Molecular imaging of water binding state and diffusion in breast cancer using diffuse optical spectroscopy and diffusion weighted MRI," J. Biomed. Opt. **17**, 071304 (2012).
[33]S. Merritt, G. Gulsen, G. Chiou, Y. Chu, C. Deng, A. E. Cerussi, A. J. Durkin, B. J. Tromberg, and O. Nalcioglu, "Comparison of water and lipid content measurements using diffuse optical spectroscopy and MRI in emulsion phantoms," Technol. Cancer Res. Treat. **2**, 563–569 (2003).
[34]Y. Guo, Y. Q. Cai, Z. L. Cai, Y. G. Gao, N. Y. An, L. Ma, S. Mahankali, and J. H. Gao, "Differentiation of clinically benign and malignant breast lesions using diffusion-weighted imaging," J. Magn. Reson. Imaging **16**, 172–178 (2002).
[35]H. P. Schwan and K. R. Foster, "Microwave dielectric properties of tissue: Some comments on the rotational mobility of tissue water," Biophys. J. **17**, 193–197 (1977).
[36]J. L. Schepps and K. R. Foster, "The UHF and microwave dielectric properties of normal and tumour tissues: Variation in dielectric properties with tissue water content," Phys. Med. Biol. **25**, 1149–1159 (1980).
[37]U. Kaatze, "On the existence of bound water in biological systems as probed by dielectric spectroscopy," Phys. Med. Biol. **35**, 1663–1681 (1990).
[38]K. R. Foster, J. L. Schepps, and H. P. Schwan, "Microwave dielectric relaxation in muscle: A second look," Biophys. J. **29**, 271–281 (1980).
[39]A. S. Hoffman, "Hydrogels for biomedical applications," Adv. Drug Delivery Rev. **944**, 3–12 (2002).
[40]N. Jouon, M. Rinaudo, M. Desbrieres, and J. Desbrieres, "Hydration of hyaluronic acid as a function of the counterion type and relative humidity," Carbohydr. Polym. **26**, 69–73 (1995).
[41]M. Lazebnik, L. McCartney, D. Popovic, C. B. Watkins, M. J. Lindstrom, J. Harter, S. Sewall, A. Magliocco, J. H. Booske, M. Okoniewski, and S. C. Hagness, "A large-scale study of the ultrawideband and microwave dielectric properties of normal breast tissue obtained from reduction surgeries," Phys. Med. Biol. **52**, 2637–2656 (2007).
[42]B. A. Brooksby, B. W. Pogue, S. Jiang, H. Dehghani, S. Srinivasan, C. Kogel, T. D. Tosteson, J. Weaver, S. P. Poplack, and K. D. Paulsen, "Imaging breast adipose and fibroglandular tissue molecular signatures using hybrid MRI-guided near-infrared spectral tomography," Proc. Natl. Acad. Sci. U.S.A. **103**, 8828–8833 (2006).
[43]A. H. Golnabi, P. M. Meaney, and K. D. Paulsen, "Tomographic microwave imaging with incorporated prior spatial information," IEEE Trans. Microwave Theory Tech. **PP**(99), 1–8 (2013).
[44]A. H. Golnabi, P. M. Meaney,and K. D. Paulsen, "Comparison of no-prior and soft-prior regularization in biomedical microwave imaging," Int. J. Med. Phys. **36**, 159–170 (2011).
[45]Y. Lin, W. C. Barber, J. S. Iwanczyk, W. Roeck, O. Nalcioglu, and G. Gulsen, "Quantitative fluorescence tomography using a combined tri-modality FT/DOT/XCT system," Opt Express **18**(8), 7835–7850 (2010).
[46]Q. Fang, J. Selb, S. A. Carp, G. Boverman, E. L. Miller, D. H. Brooks, R. H. Moore, D. B. Kopans, and D. A. Boas, "Combined optical and X-ray tomosynthesis breast imaging," Radiology **258**(1), 89–97 (2011).
[47]Q. Fang, S. A. Carp, J. Selb, G. Boverman, Q. Zhang, D. B. Kopans, R. H. Moore, E. L. Miller, D. H. Brooks, and D. A. Boas, "Combined optical imaging and mammography of the healthy breast: Optical contrast derived from breast structure and compression," IEEE Trans. Med. Imaging **28**(1), 30–42 (2009).
[48]Q. Zhu, M. Huang, N. Chen, K. Zarfos, B. Jagjivan, M. Kane, P. Hedge, and H. S. Kurtzman, "Ultrasound-guided optical tomographic imaging of malignant and benign breast lesions: Initial clinical results of 19 cases," Neoplasia **5**(5), 379–388 (2003).
[49]Q. Zhu, P. U. Hegde, A. Ricci, M. Kane, E. B. Cronin, Y. Ardeshirpour, C. Xu, A. Aguirre, H. S. Kurtzman, P. J. Deckers, and S. H. Tannenbaum, "Early-stage invasive breast cancers: Potential role of optical tomography with US localization in assisting diagnosis," Radiology **256**(2), 367–378 (2010).
[50]V. Ntziachristos, A. G. Yodh, M. D. Schnall, and B. Chance, "MRI guided diffuse optical spectroscopy of malignant and benign breast lesions," Neoplasia **4**(4), 347–354 (2002).
[51]V. Krishnaswamy, K. E. Michaelsen, B. W. Pogue, S. P. Poplack, I. Shaw, K. Defrietas, K. Brooks, and K. D. Paulsen, "A digital x-ray tomosynthesis coupled near infrared spectral tomography system for dual-modality breast imaging," Opt. Express **20**(17), 19125–19136 (2012).
[52]K. Michaelsen, V. Krishnaswamy, B. W. Pogue, S. P. Poplack, and K. D. Paulsen, "Near-infrared spectral tomography integrated with digital breast tomosynthesis: Effects of tissue scattering on optical data acquisition design," Med. Phys. **39**(7), 4579–4587 (2012).
[53]C. M. Carpenter *et al.*, "Image-guided optical spectroscopy provides molecular-specific information *in vivo*: MRI-guided spectroscopy of breast cancer hemoglobin, water, and scatterer size," Opt. Lett. **32**(8), 933–935 (2007).
[54]M. A. Mastanduno, K. E. Michaelsen, S. C. Davis, S. Jiang, B. W. Pogue, and K. D. Paulsen, "Combined magnetic resonance imaging and near-infrared spectral imaging," in *Emerging Imaging Technologies in Medicine*, Imaging in Medical Diagnosis and Therapy Series, edited by M. A. Anastasio and P. La Riviere (CRC, London, UK, 2013), Chap. 17, pp. 263–278.
[55]M. Pakalniskis, W. A. Wells, M. Schwab, H. Froehlich, S. Jiang, Z. Li, T. Tosteson, S. P. Poplack, P. A. Kaufman, K. D. Paulsen, and B. W. Pogue,

"Tumor angiogenesis change estimation by diffuse optical spectroscopic tomography: Can a correlation predict neo-adjuvant chemotherapy response in women with invasive breast cancer?," Radiology **259**(2), 365–374 (2011).

[56]S. M. Aguilar, J. D. Shea, M. A. Al-Joumayly, B. D. Van Veen, N. Behdad, and S. C. Hagness, "Dielectric characterization of PCL-based thermoplastic materials for microwave diagnostic and therapeutic applications," IEEE Trans. Biomed. Eng. **59**, 627–633 (2012).

[57]N. R. Epstein, A. H. Golnabi, P. M. Meaney, and K. D. Paulsen, "Microwave dielectric contrast imaging in a magnetic resonant environment and the effect of using magnetic resonant spatial information in image reconstruction," in *Proceedings of the 33rd Annual International Conference of the IEEE Engineering in Medicine and Biology Society, Boston, MA, 2011* (IEEE, Piscataway Township, NJ, 2011), pp. 5738–5741.

[58]T. M. Grzegorczyk, P. M. Meaney, P. A. Kaufman, R. M. diFlorio-Alexander, and K. D. Paulsen, "Fast 3-D tomographic microwave imaging for breast cancer detection," IEEE Trans. Med. Imaging **31**, 1584–1592 (2012).

[59]G. E. P. Box and D. R. Cox, "Analysis of transformations," J. R. Stat. Soc. Ser. B (Methodol.) **26**, 211–252 (1964).

[60]T. M. Grzegorczyk, P. M. Meaney, S. I. Jeon, S. D. Geimer, and K. D. Paulsen, "Importance of phase unwrapping for the reconstruction of microwave tomographic images," Biomed. Opt. Express **2**, 315–330 (2011).

[61]T. Rubaek, P. M. Meaney, and K. D. Paulsen, "A contrast source inversion algorithm formulated using the log-phase formulation," Int. J. Antennas Propag. **2011**, 849894 (2011).

[62]H. Kim, J. Lee, S. Jeon, and H. Choi, "Design and fabrication of a receiver for microwave tomography breast imaging system," in *Proceedings of the IEEE Conference on Communication Technology Convergence*, Jeju, South Korea, 2012.

[63]K. D. Paulsen and P. M. Meaney, "Compensation for nonactive array element effects in a microwave imaging system: Part I. Forward solution vs. measured data comparison," IEEE Trans. Med. Imaging **18**, 496–507 (1999).

[64]P. M. Meaney, K. D. Paulsen, B. W. Pogue, and M. I. Miga, "Microwave image reconstruction utilizing log-magnitude and unwrapped phase to improve high-contrast object recovery," IEEE Trans. Med. Imaging **20**, 104–116 (2001).

[65]P. M. Meaney, K. D. Paulsen, and T. P. Ryan, "Two-dimensional hybrid element image reconstruction for TM illumination," IEEE Trans. Antennas Propag. **43**, 239–247 (1995).

[66]P. M. Meaney, K. D. Paulsen, and J. T. Chang, "Near-field microwave imaging of biologically based materials using a monopole transceiver system," IEEE Trans. Microwave Theory Tech. **46**, 31–45 (1998).

[67]Q. Fang, P. M. Meaney, and K. D. Paulsen, "Viable three-dimensional microwave imaging: Theory and experiments," IEEE Trans. Antennas Propag. **58**, 449–458 (2010).

[68]D. Li, P. M. Meaney, T. Raynolds, S. A. Pendergrass, M. W. Fanning, and K. D. Paulsen, "A parallel-detection microwave spectroscopy system for breast imaging," Rev. Sci. Instrum. **75**, 2305–2313 (2004).

[69]P. M. Meaney, F. Shubitidze, M. W. Fanning, M. Kmiec, N. R. Epstein, and K. D. Paulsen, "Surface wave multipath signals in near-field microwave imaging," Int. J. Biomed. Imaging **2012**, 697253 (2012).